4 ANALOG VLSI SYSTEM FOR ACTIVE DRAG REDUCTION

Vincent Koosh, Bhusan Gupta, Dave Babcock,
Rodney Goodman, Fukang Jiang, Yu-Chong Tai,
Steve Tung[†] and Chih-Ming Ho[†]

Dept. of Electrical Engineering
California Institute of Technology, Pasadena, CA 91125
{darkd,bgupta,babcock,rogo}@micro.caltech.edu

[†]Department of Mechanical and Aerospace Engineering
University of California, Los Angeles CA 90024

We describe an analog CMOS VLSI system that can process real-time signals from shear stress sensors to detect regions of high shear stress along a surface in an airflow. The outputs of the CMOS circuit control the actuation of micromachined flaps with the goal of reducing this high shear stress on the surface and thereby lowering the total drag. We have designed, fabricated, and tested parts of this system in a wind tunnel in both laminar and turbulent flow regimes. The implemented system includes adaptive circuits for temperature stabilization in the shear stress microsensors and global gain control in the microactuators.

4.1 INTRODUCTION

In today's cost-conscious air transportation industry, fuel costs are a substantial economic concern. Drag reduction is an important way to increase fuel efficiency which reduces these costs. Even a 5% reduction in drag can translate into estimated savings of millions of dollars in annual fuel costs.

Organized structures which play an important role in turbulence transport may cause large skin friction drag. Commonly observed near-wall streamwise vortices cause high drag in turbulent flows (Figure 4.1). The interaction of these vortices,
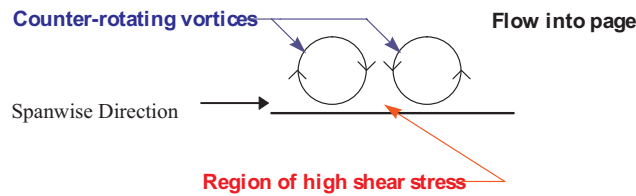
81

Figure 4.1   Diagram of the interaction between a vortex pair and the wall showing the high shear stress (hence drag) region created by the pair of counter- rotating streamwise vortices.

which appear randomly in both space and time, with the viscous layer near a surface creates regions of high surface shear stress. This shear stress, when integrated over a surface, contributes to the total drag. Attempts to reduce drag by controlling turbulent flows have focused on methods of either preventing the formation or mitigating the strength of these vortices. The microscopic size of these vortices, which decreases as the Reynolds number of the flow increases, has limited physical experimentation, and the inherent complexity of the non-linear Navier-Stokes equations has likewise limited the analytical approaches.
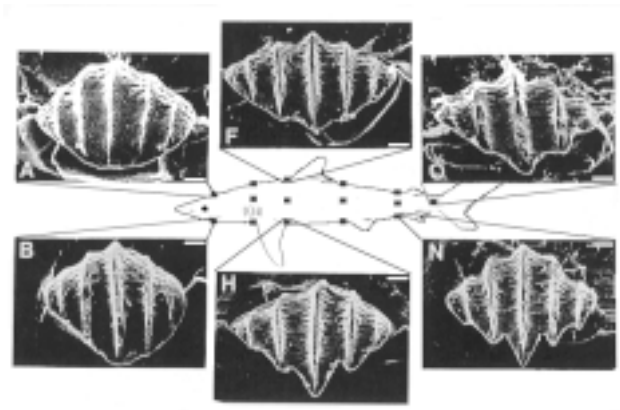
4.2   CAN BIOLOGY TELL US SOMETHING?

Figure 4.2   Examples of shark scales (white bar = 25 μm).

In many complex problems, one can often find inspiration by observing how nature has evolved biological systems to address the problem. For drag reduction, deep sea

sharks serve as a potential biological model because they are a highly evolved predator with a 350 million year old lineage. Deep-sea sharks (for example, hammerhead sharks) can swim up to 20 meters per second (72 km per hr) in deep water. The exact physiology of these species remains a mystery because they are difficult to study as the deep sea setting is hard to replicate in a controlled environment. Biologists do know, however, something about the scales (dermal denticles) that cover the shark's skin. Only recently researchers [1] found that the denticles have microscopic structure to them (Figure 4.2). The natural argument about evolution would lead one to conclude that the structure of these scales assists the sharks' movement, perhaps indicating some method of drag reduction.

4.2.1 Active Control

The entire question of active control of shark skin is very much a speculative one. Biologists hypothesize [2] that sharks can actively move their denticles. The indirect evidence of this is twofold. One, the denticles connect to muscles underneath the shark's skin. Two, the total number of mechano-receptive pressure sensors (pit organs) and their placement on a shark's body positively correlates with the speed of the species. For good active control the shark may need many sensors to relay the current condition over its body. However, questions remain about sharks utilizing active control. The conclusion that one can draw from this example of biology is that it may be beneficial to employ controlled microscopic structures to reduce the drag.

4.3 HOW SMALL IS SMALL?

By examining drag patterns in our wind tunnel at velocities between 10 and 20 m/s (36 and 72 km/hr), one can narrow the scope of the problem in order to extract useable statistics. The drag-inducing vortex pair streaks vary as the Reynolds number of the flow changes. For a typical airflow of 15 meters per second (54 km/hr) in the wind tunnel, the Reynolds number is about 104. This, in turn, gives the vortex streaks a statistical mean width of about 1 millimeter. The length of a typical vortex streak can be about 2 centimeters giving the streaks a twenty to one aspect ratio. The average spacing between streaks is about 2.5 millimeters. The mean rate of appearance of the streaks is approximately 100 Hz. The appearance and disappearance of these vortex pairs can best be described by a chaotic process.

4.4 NEURAL NETWORK BASED CONTROL

Previous numerical simulations [3] demonstrated that suppressing the interaction between streamwise vortices and the wall achieves significant drag reduction (on the order of about 25%). These computational fluid dynamics' experiments incorporate
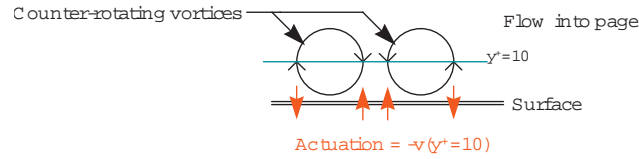
Figure 4.3   Simple control law which demonstrates the required actuation at the wall boundary to achieve a significant drag reduction.

active feedback control to achieve this goal. The control scheme used in the experiments involved blowing and suction at the wall according to the normal component of the velocity field. This normal component ($-v(y^+ = 10)$) is sensed in the near-wall region away from the surface (see Figure 4.3). The problem with these techniques is that it requires information about the velocity away from the wall. This information is very difficult to obtain in a real system.
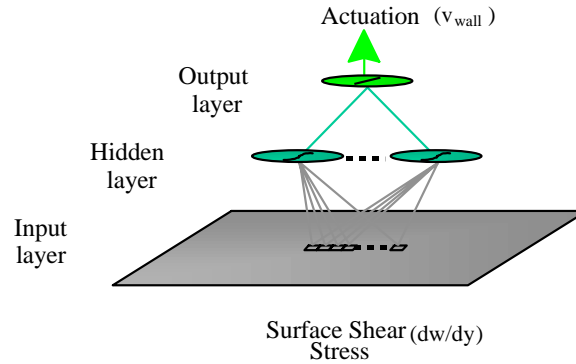

Figure 4.4   Neural Network Architecture.

Thus, an adaptive controller based on a neural network [10] that does not require velocity information away from the wall was implemented. A two layer shared weight neural network consisting of hyperbolic tangent non-linear hidden units and linear output units to predict similar actuation using only surface measurable quantities, i.e. surface shear stresses, was developed (Figure 4.4). Training off-line with data from the near-wall controlled experiments, the neural network extracted a pattern that predicts the local actuation to be proportional to the spanwise derivative of the spanwise shear stress in the surrounding region (Figure 4.6). The same network was then applied at each grid point in the input (surface spanwise shear stress) array to generate the corresponding output (actuation) array.
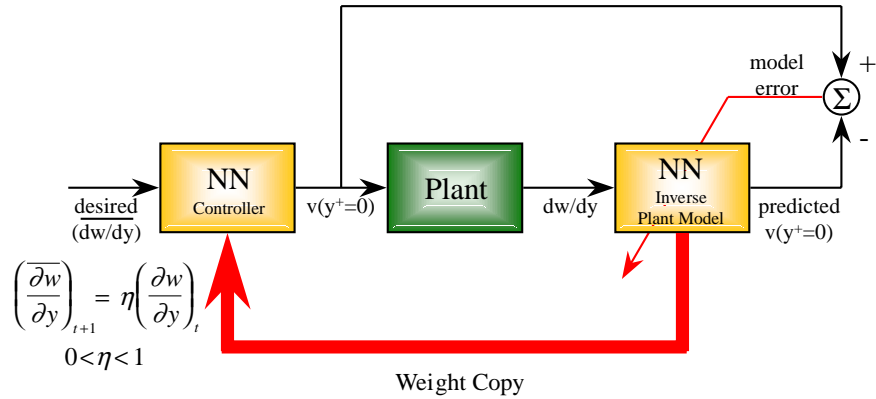
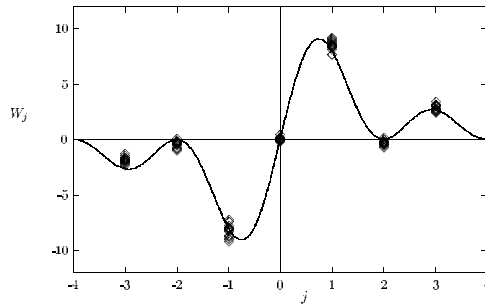Figure 4.5   Adaptive Inverse Model Scheme for Neural Controller

Figure 4.6   Learned Weight Pattern. $W_j = A \frac{1 - \cos \pi j}{j}$

This neural controller was applied in an on-line adaptive inverse model scheme (Figure 4.5) We observed that the relative magnitudes of the weights did not change (indicating the approximate derivative pattern is preserved) but that the absolute magnitudes fluctuated during the course of the simulation. Therefore the input weights were fixed to compute an approximation to the derivative leaving only a gain and bias for each layer to adapt as the simulation progresses.

Applying this control network and employing blowing and suction at the wall based only on the wall shear stresses in the spanwise direction, was shown to reduce the skin friction by as much as 20% in direct numerical simulations of a low-Reynolds number turbulent channel flow (Figure 4.7). Also, since a stable pattern was observed in the distribution of weights associated with the neural network, it was possible to derive a simple control scheme that produced the same amount of drag reduction. This
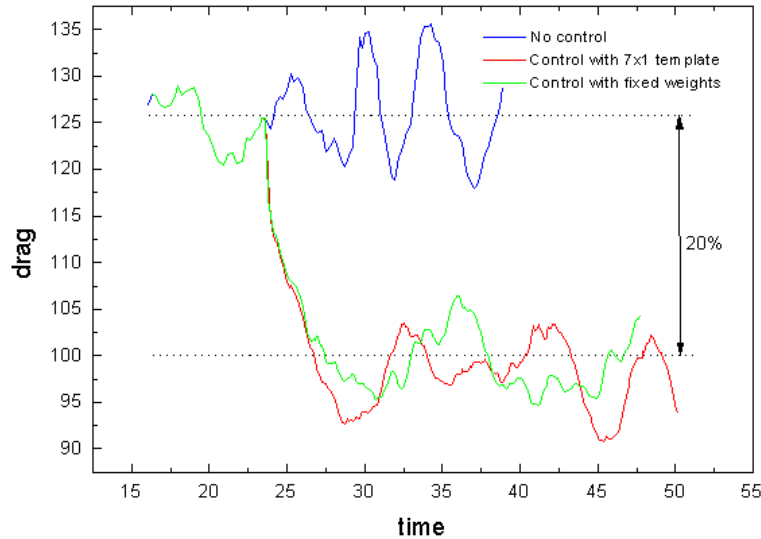
Figure 4.7   Numerical experiment of skin friction reduction

simple control scheme generates optimum wall blowing and suction proportional to a local sum of the wall shear stress in the spanwise direction. The distribution of corresponding weights is simple and localized, thus making real implementation more straightforward.

Although this work is a significant improvement over earlier approaches that require velocity information within the flow, there are still a number of technical issues before such a control scheme can be implemented in real practice. Among other things, precise control of blowing and suction distributed over a surface in a laboratory test is still too difficult to implement.

However, it appears that a simple control law that pushes the areas of high shear stress away from the wall is beneficial to minimizing the overall drag. This observation forms the basis for the system that we wish to build.

4.5   SYSTEM DETAILS

We want to combine the technologies of silicon micromachining and analog VLSI to build an integrated system which actively strives to reduce the drag along its surface.
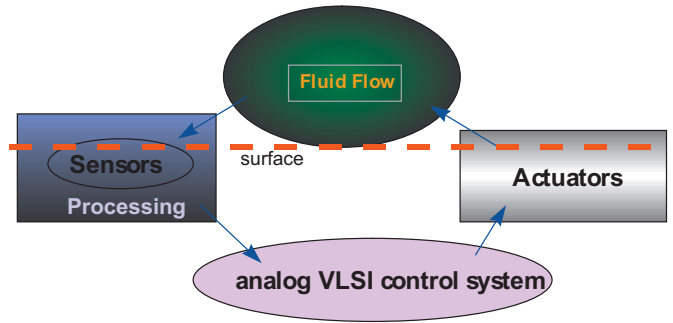
Figure 4.8   Schematic diagram of our proposed system.

Micromachining technology allows construction of fluid sensors and actuators on the same scale as the vortex pairs. Analog VLSI affords us the ability to build dense circuits which do the real-time processing necessary for an integrated system.

The goal is to design a system (Figure 4.8) that incorporates VLSI control circuitry along with microscopic sensors and actuators and control circuitry that can actively deform its surface to reduce drag.
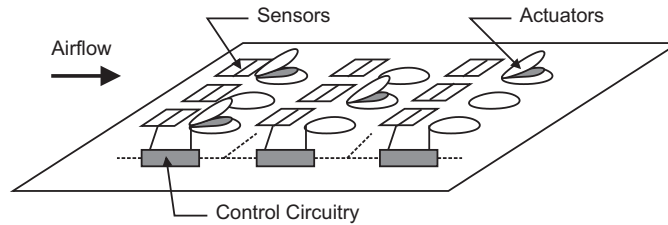

Figure 4.9   Simplified diagram of the hardware system.

Figure 4.9 shows the desired physical layout of our system — both sensors and actuators cover the surface controlled by circuitry underneath.

Circuits process the signals from the sensors to find regions of high shear stress. This detection process uses information about the spatial and temporal nature of the streaks. First, the long and narrow aspect ratio leads to building "column"-oriented templates for streak detection. We organize the sensor outputs into thin feature detectors oriented in the direction of the airflow. When several sensors in a column register either a larger or smaller output than their neighbors in a spanwise direction, this difference accumulates. If this accumulated difference exceeds a threshold, a vortex pair streak may be present in that column. The appropriate control action raises the associated actuator.

4.6 MICROMACHINED COMPONENTS

The microsensors and microactuators [4,5,6,11] employ silicon micromachining technology.

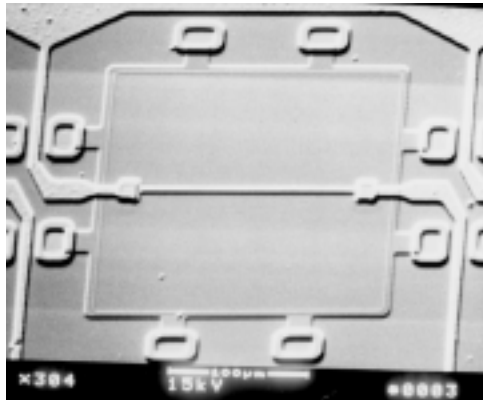### *4.6.1 Shear Stress Sensor*

Figure 4.10   Shear stress sensor showing polysilicon wire over diaphragm.

The microsensor (Figure 4.10) allows measurement of the heat transfer between a heated wire and the air. Heat transfers by convection from the electrically heated wire to the fluid flow causing a power change in the polysilicon wire. The polysilicon wire sits on a 200 μm square, 1.2 μm thick silicon nitride diaphragm over a vacuum cavity. The 2.0 μm deep vacuum cavity serves to minimize thermal losses to the substrate. The sensitivity of the sensor with a cavity underneath is on the order of 10's of mV/Pa. This is approximately an order of magnitude larger than what is attainable without the cavity.

A discrete constant temperature (CT) circuit (Figure 4.11) controls the shear stress sensor. The circuit maintains a constant temperature on the heated wire by means of balancing a bridge. The amplified voltage feedback signal is the output. The overall gain of the CT circuit is about 20.

We build the sensors as one row of 25 sensors (Figure 4.12). This allows monitoring of a spanwise section of the wind tunnel. Five sensor outputs (in the middle) provide inputs to the detection/control chip. Because we have many fewer actuators than sensors, it is unnecessary to use more sensors in the detection experiments.
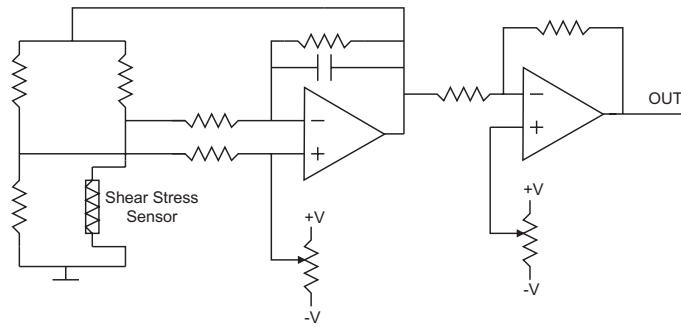
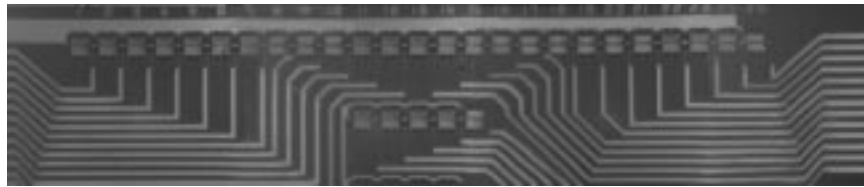Figure 4.11   Constant Temperature Circuit for the Shear Stress Sensor
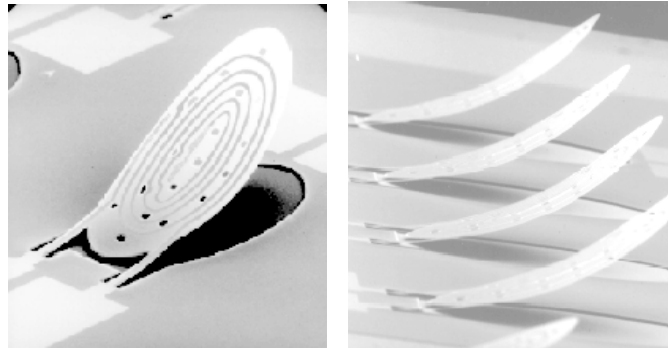

Figure 4.12   Array of shear stress sensors.

Figure 4.13   Photograph of a microactuator and an array of microactuators.

4.6.2   *Microactuator*

The microactuator (Figure 4.13) [7] is a thin plate raised via magnetic actuation. Current through a coil of metal in the external magnetic field is enough to cause millimeters of deflection.
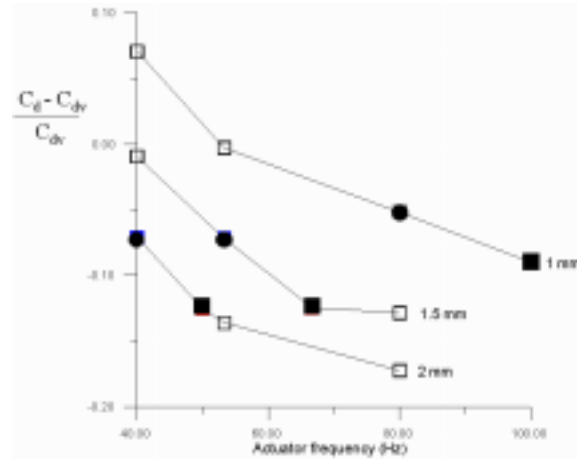
Figure 4.14   Variation of the shear stress coefficient, C_{DN}, with actuator frequency, ω, and maximum actuator tip height, d. The solid O markers correspond to an ωd of 80 and the solid square markers correspond to an ωd of 100.

How the motion of the streamwise vortices is affected by the actuator and eventually achieves skin-friction reduction is a key issue for interactive wall flow control. Experiments have been carried out to investigate the interaction between a single high shear-stress streak and a micromachined actuator(Figure 4.14). Experiments are performed for different combinations of actuator frequency (ω) and maximum tip height (d). As expected, the non-linear interaction between a moving surface and a vortex is complex. On the other hand, skin-friction reduction can be achieved if the actuation is properly applied. The reduction is a function of the product of ω and d. Since the product of ω and d is a measurement of the transverse velocity of the actuator flap, this result indicates that the amount of shear stress reduction is directly related to the transport of high-speed fluid away from the surface by the vertical motion actuator.

4.7   EDGE DETECTION/CONTROL CIRCUITS

The first control circuits that were developed were only loosely based on what was learned from the neural network simulation. Their main goal was to detect a large enough edge in the shear stress profile which would then activate the actuators. Figure 4.15 shows a diagram of how the information flows in the edge detection/control chip. A non-linear filtering network connects together the amplified outputs of the shear stress sensors. The filtering preserves large differences between adjacent sensors while smoothing away small differences. The comparison and aggregation operations
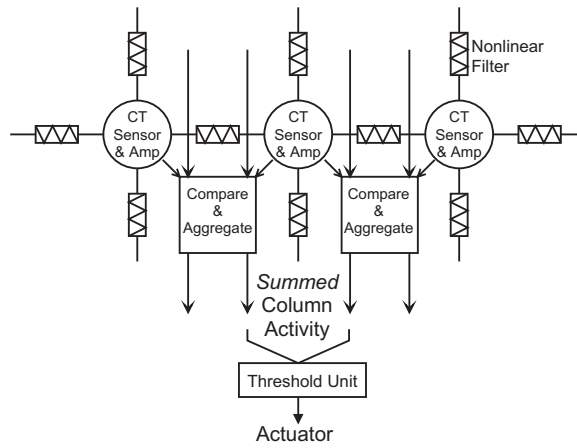
Figure 4.15   Block diagram of the complete edge detection/control chip.

correspond to different actuators by columns. Once the aggregated signal exceeds a threshold, the system drives the actuator.
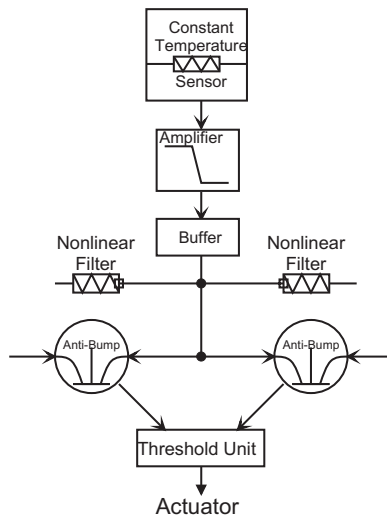
Figure 4.16   Schematic of one column (channel) of the threshold detection/control circuitry

Figure 4.16 depicts a detailed schematic of a single column (or channel). The CT output sensor signal feeds into a further stage of amplification (Figure 4.17). A buffer (Figure 4.18) distributes the amplified signal to a non-linear resistive network composed of the HRES circuits [8] (Figure 4.19). Sensor outputs in the same column and sensor outputs in adjacent columns use different spatial filtering constants. The different constants serve to reinforce activity within a column and discourage activity between adjacent columns. The filtered signals feed to a symmetric anti-bump circuit [9] (Figure 4.20). The circuit's operation mimics a soft comparator with an adjustable dead zone. The function of the circuit is to indicate when a particular column has registered a large shear stress value while the neighboring columns have not. The output of the anti-bump circuit, a current, accumulates for a particular column and compared to a threshold using the circuit in Figure 4.21. If the accumulated value exceeds the threshold, the circuit triggers the actuator by turning on a pull-down transistor.
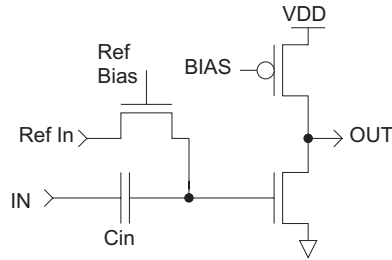

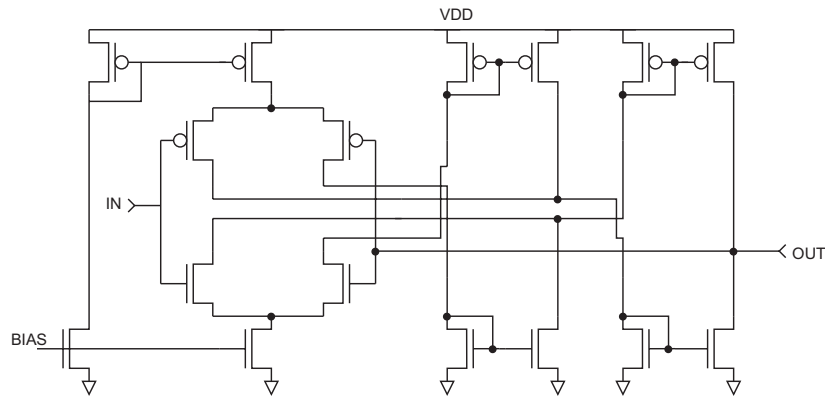Figure 4.17   Schematic of the first stage amplifier.

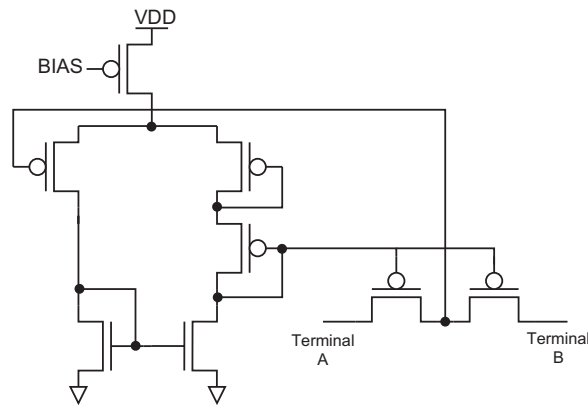Figure 4.18   Schematic of a rail to rail buffer amplifier.

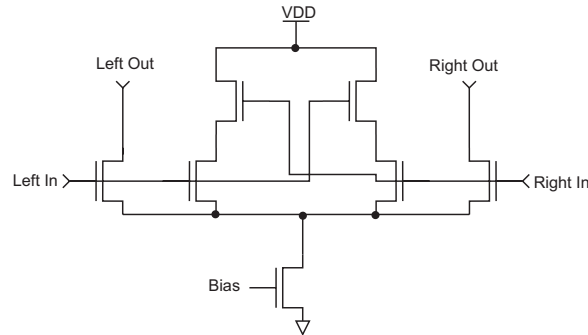Figure 4.19   Schematic of the nonlinear resistor (HRES).

Figure 4.20   Schematic of the symmetric anti-bump/comparator circuit

The edge detection/control chip was fabricated using the 2.0μm CMOS process available through Mosis (Orbit Semiconductor N-Well). Figure 4.22 shows the chip plot.

4.7.1   System Testing

Several different experiments can test various components of the system. First, signal generators present synthetic signals to the edge detection/control chip to validate the outputs. Second, mechanical actuators generate known disturbances to verify the response of the system operating in the laminar regime of the wind tunnel. Third, the system interacts with a fully turbulent channel flow in the wind tunnel to observe the response of the system.
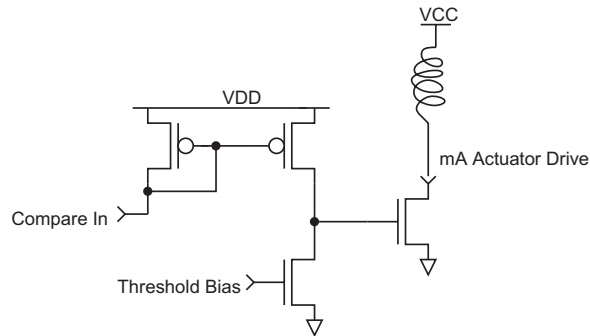
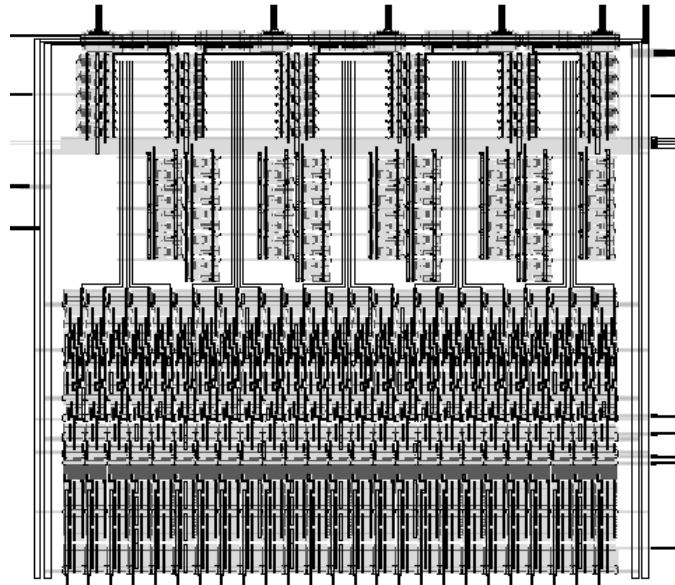Figure 4.21   Schematic of the threshold comparator circuit.

Figure 4.22   Plot of the edge detection/control chip.

Lab bench results.   The overall delay of the processing system is about 40 μs. The amplifier in Figure 4.17 has a gain-bandwidth product of approximately 500 kHz with the transistors operating in the subthreshold region. The buffer (Figure 4.18) has a full power bandwidth of 100 kHz. We set the HRES bias to 0.5 V which corresponds to minimal spreading. We also set the anti-bump circuit bias for a 160 mV dead zone.

The delay of the circuits in Figure 4.20 and Figure 4.21 accounts for the remainder of the time delay. The actuator driver can sink about 30 mA at a 1 V drop.

Sample test of system in laminar flow. This experiment consisted of generating a periodic disturbance in a laminar flow in order to check the response of the signal processing and the actuator movement. A macro-sized actuator driven by a signal generator created the disturbance. The perturbation frequency is about seven hertz which is reasonable for the microactuator to respond. Figure 4.23 shows this experiment.
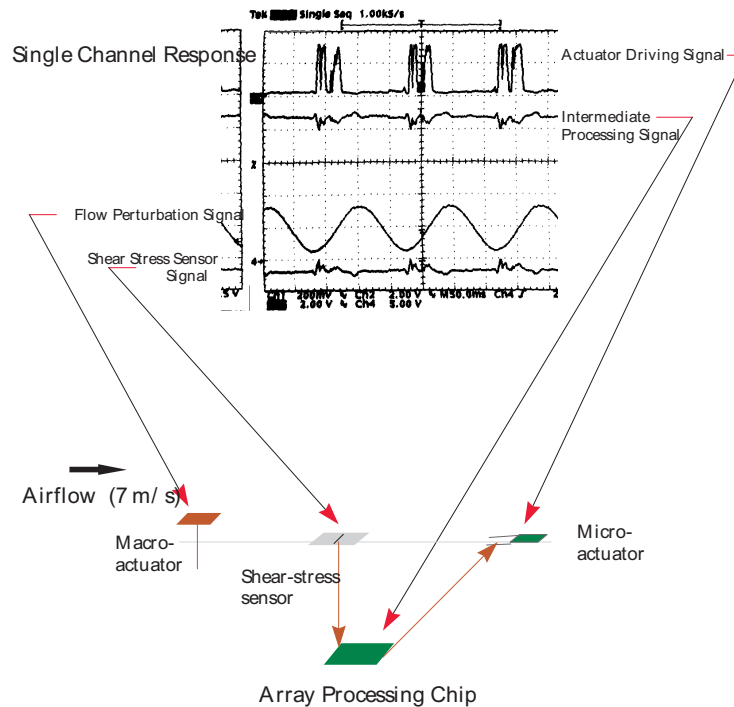

Figure 4.23   Laminar flow perturbation experiment that demonstrates the ability of the sensor plus electronics to detect disturbances in the laminar flow caused by a periodic actuation.

Another experiment we conducted is to ensure that the microactuators can, in fact, reduce drag. We conduct this experiment (depicted in Figure 4.24) in the laminar flow regime with an artificially generated vortex pair. Using a periodic driving signal on the actuators, we measured about a 10% reduction in the averaged shear stress. This

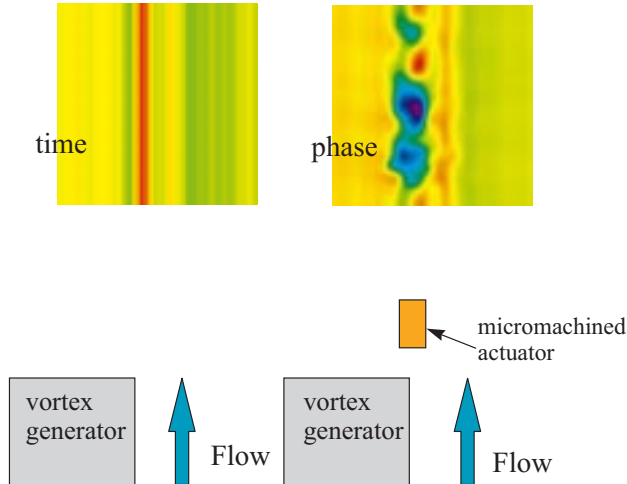result, however, does not include the consideration of form drag which would reduce the effectiveness.

Figure 4.24   Demonstration of the effect a microactuator can have on an artificially generated vortex in a laminar flow. The averaged shear stress on the right-hand plot is approximately 10% less as compared to no actuation plot on the left-hand side.

Turbulent Drag Performance.   We designed this system to reduce the fully turbulent drag in our experimental setup. We present the system with a fully turbulent airflow profile. The centerline velocity of our wind-tunnel channel varies between 10 m/s and 20 m/s (36 km/hr and 72 km/hr).

Figure 4.25 graphs the single column response of the system.

Figure 4.26 shows a plot of the full field of 25 sensors and the reduced five-sensor field used to generate the detection/control output. Figure 4.27 plots the input-output relationship between wall shear stress and the actuator activation signal. Notice that all large shear stress measurements have triggered actuator responses.

In this experiment, the microactuators do not yet have the mechanical frequency response to follow the actuation signals. Thus, only a rough estimate of the drag reduction that our system provides is possible. We record both the outputs of the shear stress sensors and the outputs of the detection/control chip. From our data, we estimate the drag reduction is approximately 2.5% assuming that the microactuators are about 75% effective in mitigating the high shear stress.
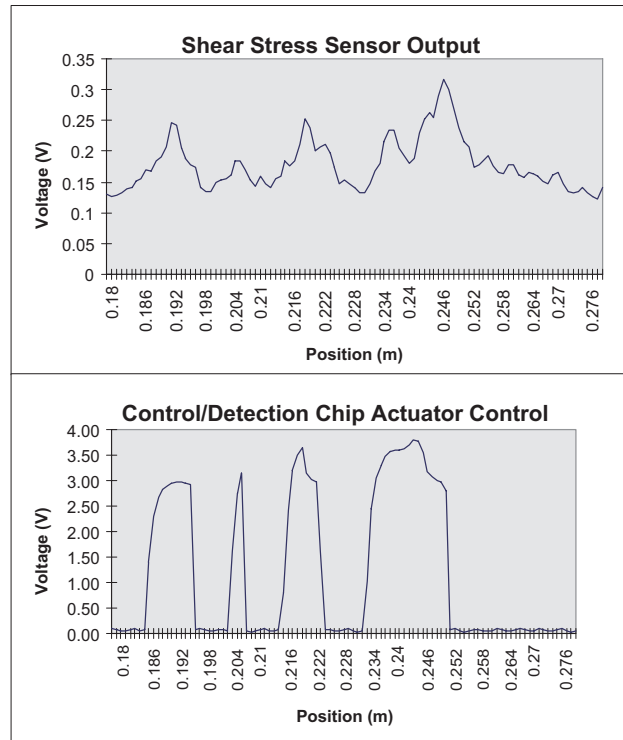
Figure 4.25   Graph of the output waveforms of one shear stress sensor and the corresponding channel from the detection/control chip. We record the data in a fully developed turbulent flow.

4.8 NEURAL NETWORK CONTROL CIRCUITS

After the initial success of the edge detection/control chip which was only roughly based on the neural network simulation results, it was decided to attempt to implement a system that utilized more of the knowledge obtained from the neural network simulations and to attempt to implement the network as closely as possible (Figure 4.28).

The previous work on the application of neural networks to turbulence control of drag reduction showed that a neural network could be trained to reduce the drag. The network that was trained was a standard two-layer feedforward network with inputs of du/dy, the streamwise shear stress, and dw/dy, the spanwise shear stress. However, during the training it was discovered that only the dw/dy inputs impacted network
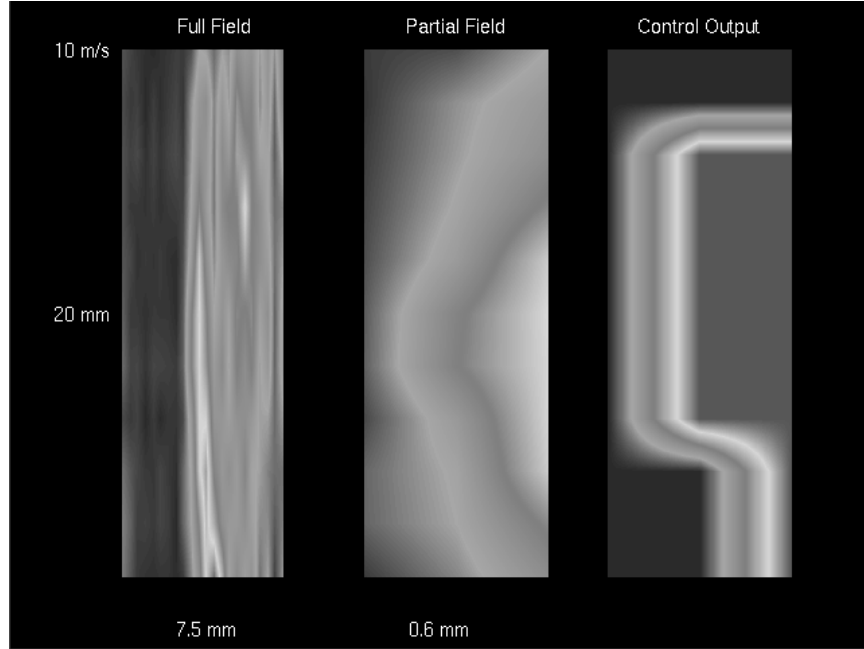
Figure 4.26   Two dimensional flow picture of instantaneous shear stress. From left to right we plot the full span (25 sensor) recording, an enlargement of the middle three sensors, and finally, the output of the detection/control chip corresponding to those three inputs. We record the data in a turbulent flow regime with a free stream velocity of 10 m/s. We obtain the two dimensional aspect of the plots by time sampling a one dimensional span

performance. The function implemented by the network is given by:

$$v_{jk} = W_a \tanh\left(\sum_{i=-3}^{3} W_i \left. \frac{\partial w}{\partial y} \right|_{j,k+i} - W_b \right) - W_c$$

where v is the velocity output at the wall and j and k denote the numerical grid point in the streamwise and spanwise directions. Also, an input template size of 7 spanwise shear stress sensors was shown to be sufficient for drag reduction. Furthermore, during the training of the network it was discovered that the weight values settled and then remained constant relative to each other but with the same scale factor applied for each.
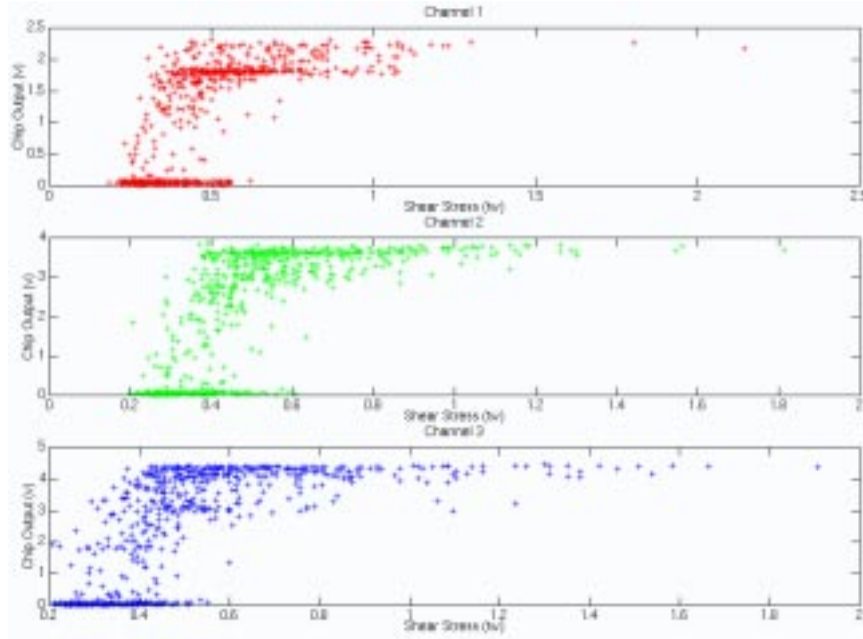
Figure 4.27   Transfer curve for three channels of the detection/control chip with the data recorded at 15 m/s. The data indicates that for large values of shear stress, the detection and control circuitry would, in fact, turn on an actuator.

The weight pattern shown in Figure 4.6 was found to be given by:

$$W_j = A \frac{1 - \cos \pi j}{j}.$$

The meaning of this weight pattern was discovered to be that the network implemented a scaled spanwise derivative of dw/dy.

Training of this network showed that W_c and W_d were negligible, and that W_a and W_b varied significantly but their product remained relatively constant. It was further discovered that a linear network produced similar results to the nonlinear one, but the standard deviation of the learned weights was worse than with the nonlinear network. Thus, the final, linear network architecture is given by:

$$v_{jk} = C \sum_{i=-3}^{3} W_i \left. \frac{\partial w}{\partial y} \right|_{j,k+i}.$$
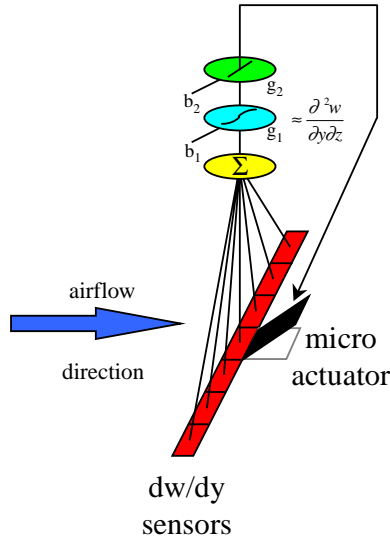
Figure 4.28   Neural network architecture.

For the linear network it was seen that the fixed weight pattern could be used, and that the scale factor, C, was dependent upon the flow velocity and could be chosen such that the root-mean-squared value of all of the actuation was kept at $0.15u_\tau$, a fixed value for a given flow velocity. Thus,

$$C = \frac{K}{\sqrt{\sum_j v_j^2}}$$

for a single row of actuators, and K is a fixed constant determined by the parameters of the flow.

This linear network significantly simplifies the circuitry necessary for implementation. Only one parameter must adapt to the flow conditions. The final system diagram for the network is shown in Figure 4.29.

In hardware, we will implement a single row of dw/dy sensors that trigger a single row of actuators. Thus the circuits used to control the actuations must be able to perform the aforementioned computations.

The dw/dy sensors come from constant temperature circuits that place them in a Wheatstone bridge configuration. The output is a voltage related to dw/dy. The first thing that must be accomplished is the summing and weighting of these voltages. The circuit in Figure 4.30 [12] is used for this purpose.

CT Sensor Voltage Inputs

$I_1 = \Sigma W_i S_i$ $I_2 = \Sigma W_i S_i$ $I_3 = \Sigma W_i S_i$

Compute RMS Normalization Constant

$I_{out1} = C(\Sigma W_i S_i)$ $I_{out2} = C(\Sigma W_i S_i)$ $I_{out3} = C(\Sigma W_i S_i)$

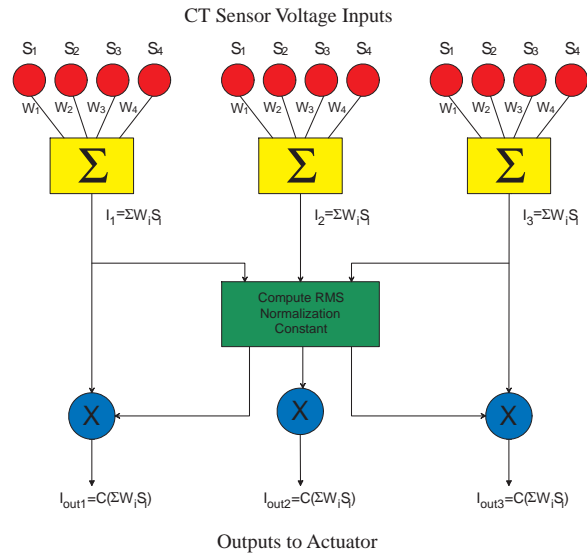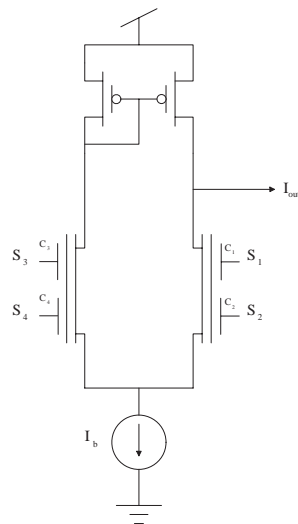Outputs to Actuator

Figure 4.29   Linear network diagram.

Figure 4.30   Circuit for computing weighted summation function.

The output of this circuit is given by $I_{out} \propto \sum_i W_i S_i$, where the S_i are the voltage inputs from the constant temperature sensor driver, and the weights, W_i are implemented as fixed capacitor ratios. The CT sensor outputs are always of the range that the weighted summation circuit always functions in its linear region. Thus, the weight pattern can be implemented by choosing the capacitor ratios to match the equation for W_j given above.

One benefit of the weight pattern is that for an input template of size 7, only 4 sensors are actually needed since the even weights are zero and nullify those sensors.

The rest of the signal processing is done in current mode since the previous stage, which does weight multiplication and summing, outputs a current. The linear network requires the output of the weighting and summing network to be scaled and normalized by the rms value of all of the other sensor arrays outputs. The building blocks of the rms circuit are shown in Figures 4.31 - 4.33.
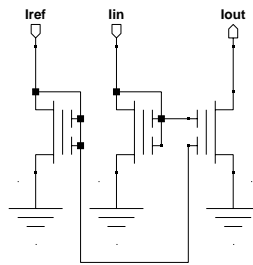

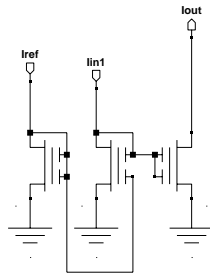Figure 4.31   Circuit for computing square root function. $I_{out} = \frac{I_{in}^2}{I_{ref}}$

Figure 4.32   Circuit for computing squaring function. $I_{out} = \sqrt{I_{in}I_{ref}}$
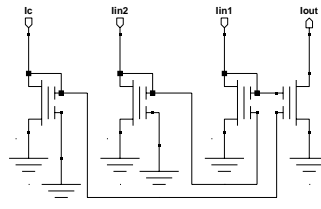
Figure 4.33   Circuit for computing division. $I_{out} = I_c \frac{I_{in1}}{I_{in2}}$

These building blocks are placed together to provide the rms normalization circuit shown in Figure 4.34.

These circuits form the core of the signal processing circuitry necessary to implement the neural networks that have only previously been implemented in software. Other circuits which are not shown are required for impedance matching between the stages, but they do not contribute to the mathematical implementation of the neural network. The final stage of processing is a current amplification stage which amplifies the currents from the small levels which are used for the analog signal processing to the larger current levels necessary to drive the actuators. This is a fixed gain stage for all signal currents to the actuators.

These circuits are all analog and perform the computations required in real-time. The linear network only requires setting I_C for the flow conditions, and the normalization circuitry provides the rest of the signal gain adjustment.

4.9   COMPLETE M^3 SYSTEM

One of the goals of this work is to implement a complete M^3 system which contains microsensors, microactuators, and microelectronics all on the same die. Figure 4.35 shows a 1cm by 1cm die with 18 micro shear stress sensors, 3 micro flap actuators as well as the edge detection circuits, sensor driver and actuator drivers all monolithically integrated. Although all of the individual subsections worked on the die, the system as a whole is not yet fully functional. One of the problems in such an endeavor is being able to obtain reliable mechanical data for the implementation of the sensors and actuators prior to fabrication. Currently, accurate models are not available making it difficult to simulate the whole system before it is fabricated. Nevertheless, the 2nd generation system is currently being tested, and plans for a 3rd generation are underway.
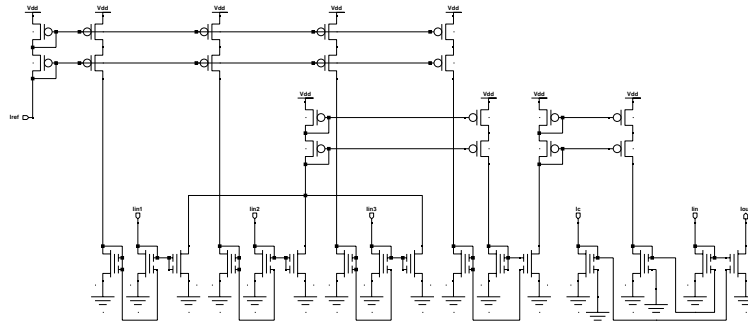
Figure 4.34   Circuit for computing RMS normalization. $I_{out} = I_c \dfrac{I_{in}}{\sqrt{I_{in1}^2 + I_{in2}^2 + I_{in3}^2}}$

4.10   CONCLUSIONS

We have described an analog VLSI system that interfaces with microfabricated constant temperature shear stress sensors. This system detects regions of high shear stress and outputs a control signal to activate a microactuator. We are in the process of verifying the actual drag reduction with a fully integrated system in wind tunnel experiments. It has been seen that neural networks are very useful for both understanding the problem, and finding a suitable implementation for a solution. We are encouraged that an approach similar to one that biology may employ provides a very useful contribution to the problem of drag reduction.
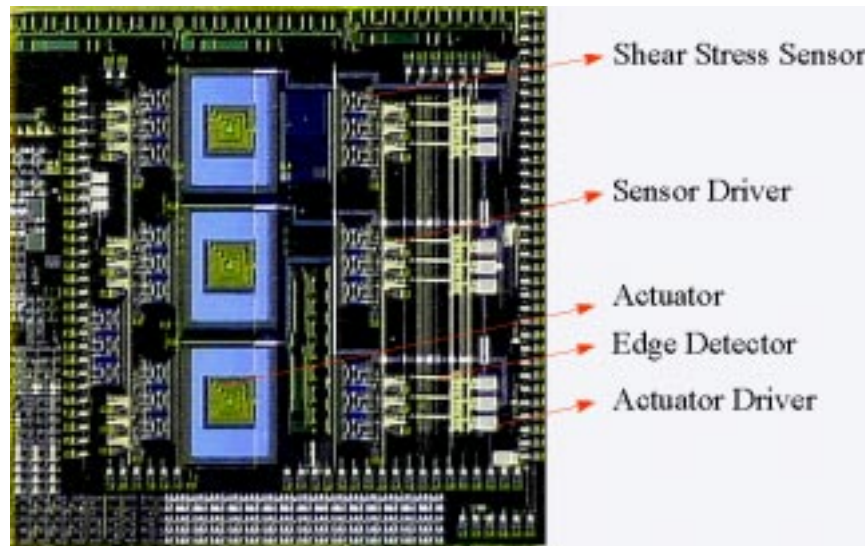
Figure 4.35   Die photograph of fully integrated system for shear stress reduction.

Acknowledgments

References

[1]   D.W. Bechert, G. Hoppe, W.-E. Reif, "On the Drag Reduction of the Shark Skin", AIAA paper No. 85-0546, 1985.

[2]   W.-E. Reif and A. Dinkelacker, "Hydrodynamics of the squamation in fast-swimming sharks", *Neues Jahrb. Geol. Paläontol. Abh.*, (1982), vol. 164, pp. 184-187.

[3]   P. Moin, J. Kim, H. Choi, "On Active Control of Wall-Bounded Turbulent Flows", AIAA Paper No. 89-0960, 1989.

[4]   P.R. Bandyopadhyah, "Development of a Microfabricated Surface for Turbulence Diagnostics and Control", *ASME Application of Microfabrication to Fluid Mechanics*, Chicago (1994), pp. 67-74.

[5]   C. Liu, Y.C. Tai, J.B. Huang, C.M. Ho, "Surface Micromachined Thermal Shear Stress Sensor", *ASME Application of Microfabrication to Fluid Mechanics*, Chicago (1994), pp. 9-15.

[6]   F. Jiang, Y.C. Tai, J.B. Huang, C.M. Ho, "Polysilicon Structures for Shear Stress Sensors", *Tech. Digest IEEE TENCON '95*, Hong Kong, Nov. 1995.

[7]   T. Tsao, C. Liu, Y.C. Tai, C.M. Ho, "Micromachined Magnetic Actuator for Active Fluid Control", *ASME Application of Microfabrication to Fluid Mechanics*, Chicago (1994), pp. 31-38.

[8]   C.A. Mead, *Analog VLSI and Neural Systems*, Addison-Wesley, Reading, Massachusetts (1989).

[9]   T. Delbrück, "Bump Circuits for computing similarity and dissimilarity of analog voltages", *Computation and Neural Systems Dept. Memo 10*, California Institute of Technology, Pasadena (1991).

[10] C. Lee, J. Kim, D. Babcock, R. Goodman, "Application of neural networks to turbulence control for drag reduction," *Physics of Fluids*, Vol. 9, No. 6, June 1997, pp. 1740-1747.

[11] Jiang, F., Tai, Y.C., Gupta, B., Goodman, R., Tung, S., Huang J., and Ho, C.M., "A Surface-Micromachined Shear-stress Imager," *Proceedings, IEEE MicroElectroMechanical Systems Meeting*, pp. 110-115, San Diego, California, Feb. 1996.

[12] Yang, K.W., Andreou A.G., "A Multiple-Input Differential-Amplifier Based on Charge Sharing on a Floating-Gate MOSFET", *Analog Integrated Circuits and Signal Processing* 6: (3) pp. 197-208, Nov. 1994.

[13] Minch BA, Diorio C, Hasler P, Mead CA, "Translinear circuits using subthreshold floating-gate MOS transistors", *Analog Integrated Circuits and Signal Processing* 9: (2) pp. 167-179, Mar. 1996.